Variable illumination in the PDS 66 protoplanetary disk

THESIS

submitted in partial fulfillment of the
requirements for the degree of

BACHELOR OF SCIENCE
in
ASTRONOMY AND PHYSICS

Author :	J. van Marrewijk
Student ID :	1644971
Supervisor :	S. Wolff, M. Kenworthy
2^{nd} corrector :	M. van Exter

Leiden, The Netherlands, June 15, 2019

Variable illumination in the PDS 66 protoplanetary disk

J. van Marrewijk

Huygens-Kamerlingh Onnes Laboratory, Leiden University
P.O. Box 9500, 2300 RA Leiden, The Netherlands

June 15, 2019

Abstract

Polarimeters have resolved dozens of protoplanetary disks in polarized intensities. Disks that exhibit variable illuminations in the outer regions provide new means of investigating the innermost regions and give valuable insight on physical processes inherent in terrestrial planet formation. The PDS 66 has a close to face-on view of its disk which inhabits ring- and gab-like structures. In this research, we further investigated these structures by using SPHERE/IRDIS polarimetric differential imaging in H- and J band to obtain the Stokes Q, U, and I image. We linked earlier found rotational timescale of roughly 22 years to a Jupiter mass-like planet in the inner disk, but we need new observations to exclude timescales shorter than our two year baseline. In addition, we probed the dust content by fitting an adjusted Henyey-Greenstein model to the scattering phase function and found a difference in g values and polarization fractions at 90° scattering angles for the north and south side of the disk at $g_{north} = 0.22$, $p_{north} = 16.33$, $g_{south} = 0.15$, and $p_{south} = 13.49$. These results, in combination with an enhanced surface brightness of $\approx 30\%$ in the north relative to the south side of the disk at scattering angles of 90°, suggest an asymmetric particle distribution throughout the disk. We further confirmed literature results on the inclination and position angle of the outer ring and found a stello-centric offset of 49.8 mas, which contradicts expectations in previous literature.

Contents

1 | Introduction

In the last decade, high-contrast imaging has resolved dozens of disks around young pre-main-sequence stars. These disks vary from cold debris disks to hot gas-rich protoplanetary disks. These disks play a substantial role in the physical processes inherent in terrestrial planet formation (C. Ginski et al., 2016 [1]). To fully understand these processes we need to closely examine these circumstellar disks. The observations of these disks are made possible by combining polarimeters with high-contrast imagers.

The Spectro-Polarimetric High contrast imager for Exoplanets REsearch (SPHERE) is such an instrument that made use of polarimeters to observe polarized light (J. Beuzit et al., 2019 [2]). The polarized light originates from Rayleigh scattering, which corresponds to scatter events form stellar light on gas molecules located in the circumstellar disk (N. Engler et al., 2017 [3]). Many observations have been made with SPHERE resulting in images containing these disks shown in polarized intensities. Exciting is that these images show variable illumination regions within these disks. Those regions, or shadows, correspond to a lesser degree of polarized light. Examples of such regions are the ringlike structures of the HD97048 (C. Ginski et al., 2016 [1]), or self-shadowing effects of an inclined inner disk (C. Poteet et al., 2018 [4]). Other examples of self-shadowing effects are cold spots on the stellar surface due to magnetic suppression of convection, or density variations in the inner disk caused by planet formation. Both phenomena would cast a shadow on the outer disk, causing gab-like structures in the surface brightness. One other stellar system that shows these asymmetries in surface brightness is the PDS 66 (S. Wolff et al., 2016 [5]).

The PDS 66 (or MP Muscae) has a near face-on view due to its low inclination, $i = 32^\circ \pm 5^\circ$ (S. Cortes et al. in 2009 [6]) and a kinematic parallax distance of $d = 98.6 \pm 0.30$ pc (Gaia Collaborations, 2018 [7]), which makes it one of the closest classic T Tauri stars (cTTs). cTTs are known as solar-like pre-main sequence stars with extensive accretion disks (H. Avenhaus et al., 2018 [8]). These major disks, and their relative close distance to our solar system makes them ideal candidates for investigating variable illuminations in circumstellar disks. S. Wolff et al. 2016 [5] state that these variable illuminations could assist in understanding the physical processes inherent in terrestrial planet formation. Combining the properties of cTTS with the close to face-on view of the disk makes the PDS 66 optimal to further understand the nature of variable illumination regions.

S. Wolff et al. in 2016 [5] started with exploring these regions by using Spectral Differential Imaging (SDI), and Angular Differential Imaging

(ADI) methods. But due to its close to face-on view of the disk, recovery of the total intensity is difficult via ADI. ADI over-subtracts disk signal due to the nature of the algorithm and thus obtains a low signal to noise ratio for the total intensity image (C. Marois et al., 2006 [9]).

The goal of this research is to continue to explore these variable illumination regions and limit the possible physical processes in the protoplanetary disk of the PDS 66 by using SPHERE data observed in 2016 by H. Avenhaus et al., 2018[8]. With this data we will:

1. Use Polarimetric Differential Imaging (PDI) to create the Stokes Q, U, and I images. With the Stokes Q, and U images we will model an adjusted Henyey-Greenstein distribution to the Scattering Phase Function (SPF) for polarized intensities. The SPF describes how dust particles scatter light, by linking the outgoing radiation to the angle between the incident and the scattered light. A difference in distribution of the SPF on the north and south side of the disk might translate to an asymmetric distribution of dust particles throughout the disk.

2. Try to obtain the disk signal, with the Stokes I image, in total intensity by using a data reduction technique called Reference Differential Imaging (RDI). The total intensity image relative to the polarized intensity image results in the polarization fraction which could give insight to local scale height, and/or asymmetrical surface densities (S. Wolff et al. 2016 [5]).

3. Compare SPHERE data with earlier processed GPI images of S. Wolff et al., 2016 [5] to obtain a rotational timescale of the shadow corresponding to dynamical timescales in the inner regions of the disk, which could lead to self-shadowing effects cast by planets roaming the inner regions of the disk.

The outline of this thesis is as follows: First in section 2, the theoretical framework including the nature of polarization and how light becomes polarized, the Henyey-Greenstein distribution, and a description on the high-contrast imager we used for our observations. Then in section 3, the Methodology. Here we introduce the data reduction techniques we used for reducing the raw data. The results we obtained on the variable illumination regions are shown in section 4. Finally, section 5 & 6 provide the discussion with future recommendations and the conclusions, respectively.

2 | Theory

In this chapter, we will discuss the theoretical framework. We start this by describing the nature of polarized light in section 2.1. Then we will discuss how light becomes polarized with reflection, section 2.2 and scattering events, section 2.3. Section 2.3 includes subsection 2.3.2 that explains how to characterize dust properties with the use of a Henyey-Greenstein function. Finally, we introduce the instrument we used for our observations, in section 2.4.

2.1 Polarized light

Light can be treated as a transverse electromagnetic wave. An electromagnetic wave is an oscillation between the Electric (E) and Magnetic (M) field perpendicular to the propagation of the wave. The preferred orientation of the electric field is defined as the polarization of light.

An excited atom emits a wave train of electromagnetic radiation roughly every 10^{-8}s (E. Hecht, Optics p330[10]). When new wave trains are emitted in a completely unpredictable orientation, and the rate of emission is fast enough to render any resulting polarization, then the light is considered as unpolarized (or sometimes called randomly polarized). When light is emitted in a predictable orientation, then we can speak of polarized light. Polarized light has three different types of polarization: Linear, Circular, and Elliptical.

Linear polarized light has a fixed orientation and amplitude in the plane of vibration of the electromagnetic wave. A wave consists of a superposition of two linear orthogonal states, which can form three different kind of combinations, corresponding to the three different types of polarizations. When the two orthogonal states are emitted in-phase, then the amplitude must be constant and thus the polarization is linear. If the two states are emitted out of phase than the light is circular or elliptical polarized. The light is circular polarized if the amplitude of the wave in the x- and y-direction are equal, otherwise, the light is elliptically polarized. The three types of polarization are shown in Figure 2.1

The mathematical approach to describe polarization is introduced by George Gabriel Stokes in 1852 (E. Hecht, Optics p374[10]). He constructed four equations which are called the Stokes parameters:

$$\boldsymbol{I} = \langle E_x^2 \rangle + \langle E_y^2 \rangle \tag{2.1a}$$

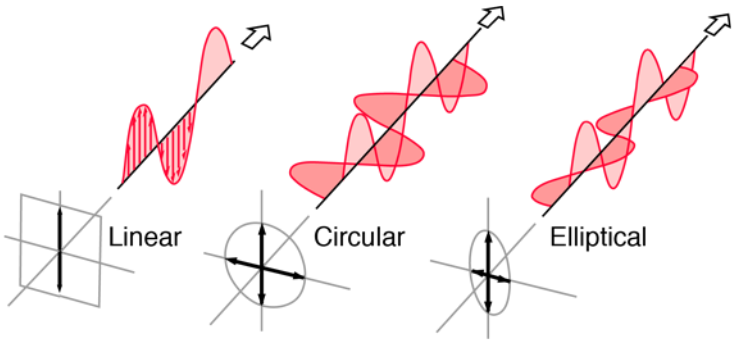

Figure 2.1: *Different kinds of polarization of the Electromagnetic field. [11]*

$$\boldsymbol{Q} = \langle E_x^2 \rangle - \langle E_y^2 \rangle \tag{2.1b}$$

$$\boldsymbol{U} = 2\mathrm{Re}(E_x E_y) \tag{2.1c}$$

$$\boldsymbol{V} = -2\mathrm{Im}(E_x E_y) \tag{2.1d}$$

Here are E_x and E_y the x- and y component of the complex electric field vector, which is also shown in Figure 2.1. I, Q, U, and V combined describe the four different kinds of polarization states. We can imagine these four vectors as a set of four unique different filters. Each filter is illuminated by natural light and transmits half the incident light. The first filter (I) will let isotropic light pass through. The second and third filter (Q, U) only pass linear polarized light with horizontal and diagonal polarization axis, respectively. We can describe the last filter (V) as a circular polarizer.

Equations 2.1b-d can be larger or smaller than zero. This corresponds for Q and U to a shift of 90° to their polarization axis. For instance, $Q < 0$ means vertical polarization and $Q > 0$ horizontal polarization. The sign of the V-vector gives the polarization angle of the intensity of light that is circular polarized. $V < 0$ is left-handed and $V > 0$ is right-handed, which corresponds to counter-clockwise and clockwise orientations, respectively (E. Hecht, Optics p374[10]).

The Stokes vector is defined as a combination of the Stokes parameters:

$$\boldsymbol{S} = (I, Q, U, V)^T \tag{2.2}$$

Each light beam has its own unique Stokes vector. When the light beam propagates through the optical path it undergoes changes in polarization states and thus creating a different set of Stokes parameters, which results in another unique Stokes vector. These alterations are defined as polarization aberrations.

2.2 Internal polarization

2.2.1 Mueller calculus

The mathematical approach to correct for internal polarization is called Mueller calculus. Mueller calculus makes use of a transformation matrix to transform one Stokes vector to another. The incoming Point Spread Function (PSF) has a unique set of Stokes parameters. When light propagates through the optical path it interacts with optical elements which cause aberration effects. This will result in different properties of the Stokes parameters. The incoming Stokes parameters are described as $\boldsymbol{S_{in}}$, with the out coming parameters as $\boldsymbol{S_{out}}$. Then the aberrations that the optical element cause to the PSF can be written as the transformation matrix M_1. This is notated as:

$$\boldsymbol{S_{in}} = M_1 \boldsymbol{S_{out}} \tag{2.3a}$$

When the light interacts with more optical elements in its path, we can describe the resulting PSF as a linear combination of single PSFs caused by aberrations of the different optical elements (J. Breckinridge et al., 2015 [12]). This results in a product of each individual transformation matrix of each optical element. So when the incoming light beam first passes through element M1, then M2 and finally element M3, we obtain:

$$\boldsymbol{S_{in}} = M_3 M_2 M_1 \boldsymbol{S_{out}} \tag{2.3b}$$

Combining all the matrices of the optical elements, with basic matrix multiplication, results in one final Mueller Matrix. The polarization aberrations to fill these Mueller Matrices result from two sources: (1) the mirror coatings necessary to make the highly reflective mirror surfaces, and (2) the optical prescription with its inevitable non-normal incidence of rays on reflecting surfaces (J. Breckinridge et al., 2015 [12]).

Currently, a team in Leiden is constructing the Mueller Matrix of the IRDIS DPI optical path. This Mueller Matrix is unfortunately not openly available yet. Thus correcting for internal Polarization effects must be achieved with a different approach. This approach is described in section 3.2.1. The origins of these aberrations are described in the next section.

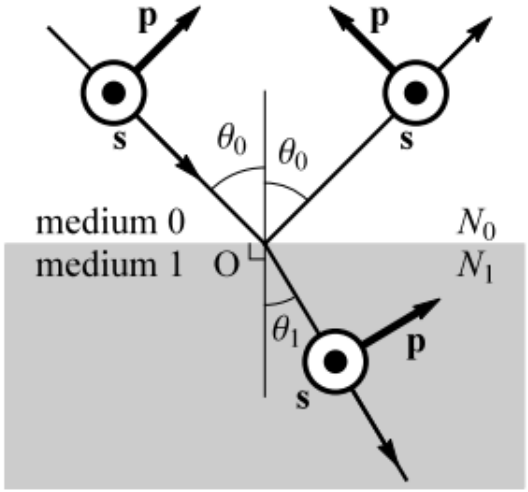

Figure 2.2: *An incident ray propagating in medium (0) of index N0 reflects from a metal mirror of index N1 at angle θ_0. The metal medium N1 is assumed optically thick. The electric field vector for the light polarized in the s direction is out of the paper, normal to the plane of incidence, and the direction vector for the light polarized in the p direction is parallel to the plane. J. Breckinridge et al., 2015, Figure 4 [12]*

2.2.2 Polarized aberrations

The mirrors in the optical path are coated with Aluminium (Al). When a plane wave is incident on this metal mirror, the electric- and magnetic radiation drive the charges in this Al coating to oscillate in the directions of the orientation of the electric field. This dipole acceleration gives rise to the reflected beam (J. Breckinridge et al., 2015 [12]).

The plane wave consists of two orthogonal components, the s- and p-component, which correspond to the x- and y- component of the complex electric field (see section 2.1). Each component containing its own Fresnel coefficient r_s and r_p, with amplitudes $|r_s|$ and $|r_p|$, and phase Φ_s and Φ_r.

$$r_p = \frac{\tan(\theta_0 - \theta_1)}{\tan(\theta_0 + \theta_1)} = |r_p| e^{i\Phi_p} \tag{2.4a}$$

$$r_s = \frac{-\sin(\theta_0 - \theta_1)}{\sin(\theta_0 + \theta_1)} = |r_s| e^{i\Phi_s} \tag{2.4b}$$

Figure 2.2 visualizes the parameters of the Fresnel equations. The frac-

tion of reflected flux is proportional to the amplitude squared and the remainder of the energy transfers to the friction of the charges moving through the metal.

The equations show that the reflection coefficients and phase of a complex wave deviate for larger refraction angles (θ_0). This difference in - components after reflection cause amplitude and phase shifts. These shifts change the polarization states of the incoming plane wave after reflection and thus acting as weak polarizers. The M3 mirror of the Nasmyth telescope has the highest reflective angle of the optical path (J. Beuzit et al, 2019 [2]) and thus causes the largest changes in amplitude and phase of the incident starlight. The section on Polarimetric Differential Imaging (section 3.2.1) explains which methods are used to correct for these polarization aberrations.

2.3 Scattered light observations

2.3.1 Scattering Angle

In the previous section, we described how light polarizes under reflection and how that could cause internal polarization aberrations inside the telescope. Here we describe how light polarizes when it is scattered off from a circumstellar disk.

Scattering is defined as the absorption and re-emission of electromagnetic radiation. Rayleigh scattering is a specific kind of scattering and is defined as the scattering of sunlight by gas or dust molecules, under the assumption that the wavelength of the radiation is larger than the grain size of the particles ($\lambda >> a$). This process is similar to the driven charges in the Al coating of section 2.2.2 and the scattering of starlight in the Earth's atmosphere. Electromagnetic radiation drives the charged gas molecules to oscillate in the orientation of the Electric field, which causes a dipole pattern that emits dipole radiation. This is illustrated on the left of Figure 2.3. It shows that the degree of polarization is angular dependent. For instance, when the scattering angle (θ), the angle between incident light and scattered light, is perpendicular to the scattering plane, then the polarization must be horizontal/azimuthal polarized.

The scattering angle we observe from protoplanetary disks is dependent on the inclination of the disk. The PDS 66 has a close to flat disk with a near face-on view (S. Wolff et al., 2016 [5]). The near face-on view makes the detection of polarized light more challenging as the thermal radiation

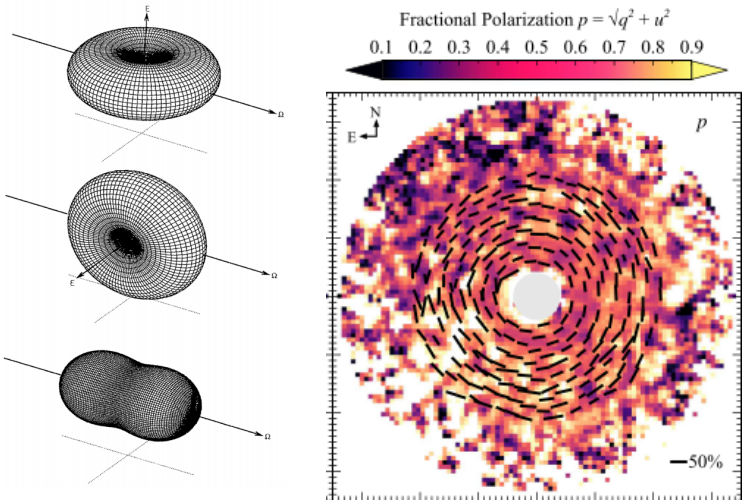

Figure 2.3: Left: *The distribution of scattered light caused by dipole radiation (under the assumption of Rayleigh scattering) of vertically polarized- (top) and horizontally polarized light (middle). Unpolarized light (bottom) is a linear combination of the two orthogonal polarized distributions (Figure 3 of University of Arizona (Griffith), 2019 [13]).* ***Right:*** *The polarization vectors of scattered starlight form the TW Hydrae disk (C. Poteet et al., 2018 [4]) follows a bullseye pattern, as scattering angles perpendicular to the scattering plane only originates from azimuthal polarizations.*

emits isotropic and can be directly detected. The scattering of this thermal radiation on the debris disk breaks the isotropic symmetry. The left of Figure 2.3 shows that the degree of linear polarized light is largest for scattering angles perpendicular to the scattering plane. This leads to bullseye patterns of the polarization vectors seen in circumstellar disks. An example of a bullseye pattern of the TW Hydrae disk is shown on the right of Figure 2.3.

The inclination is not the only geometrical effect that limits the scattering angle of the polarization vectors. It also depends on the orientation of the disk (The position angle (PA)) and the disk's flaring angle, which is defined as $\gamma = \arctan(h/r)$ with h the height of the disk at radial position r. The scattering angle can be calculated by:

$$\cos(\theta + \gamma) = \sqrt{1 - \frac{1}{1 + \cos^2(\phi - PA)\tan^2(i)}}(-1)^j \tag{2.5}$$

Where ϕ is the azimuthal angle, i the inclination, and $j = 1$ for $\cos(\phi - PA) < 0$ and $j = 0$ for $\cos(\phi - PA) > 0$ (C. Poteet et al., 2018 [4]).

We can interpret equation 2.5 as with which angle (θ) the light was scattered at position (ϕ) in the disk. The PDS 66 is expected to have a close to flat protoplanetary disk (S. Wolff et al., 2016 [5]). This translate to $\gamma \simeq 0$ as $\arctan(h/r) \to 0$, for $h/r \to 0$.

If you link θ with azimuthal angle ϕ to the surface brightness of the disk at position ϕ, you obtain the Scattering Phase Function (SPF). The SPF gives the distribution between the scattering angle and the direction of outgoing radiation. The "phase" in "scattering phase function" does not refer to the phase of the complex electric field vector of section 2.1. An example of a SPF in total intensity is shown on the left of Figure 2.4.

2.3.2 Henyey-Greenstein

In general, a phase function is used to describe the distribution of angles between incident light and the direction if outgoing radiation. The Scattering Phase Function (SPF) describes the distribution of incident light and scattered light (University of Arizona (Griffith), 2019 [13]).

A common way of interpreting the SPF, when the outgoing radiation is observed in total intensity, is by fitting a Henyey-Greenstein (HG) model to the SPF (Henyey & Greenstein, 1941 [14]). The single HG function is expressed as:

$$HG(\theta, g) = \frac{1}{4\pi} \frac{1 - g^2}{(1 - 2g\cos(\theta) + g^{2/3})^{3/2}} \tag{2.6}$$

Although the HG function has no true physical meaning, it is still the most commonly used model to interpret the behavior of dust particles. The reason is that it only depends on one parameter, g. g is defined as the average scattering angle of the dust particles, $g = \langle \cos\theta \rangle$. This translates for isotropic scattering to g = 0, g = 1 describes purely forward scattering, and for g = -1 we obtain a purely backward scattering distribution (Henyey & Greenstein, 1941 [14]). Thus determining the g-value will give insight on how dust particles scatter light and could explain a difference in surface brightness when a difference in g-values is found in specific parts of the disk.

J. Mili et al. [15] and N. Engler et al. [3] argue that fitting a single HG function would be inaccurate for modeling the dust content of the disk. They propose a 2-component HG function with a weight factor (w):

$$HG_2(\theta, g_{sca}, g_{dif}, w) = wHG(\theta, g_{sca}) + (1 - w)HG(\theta, g_{dif}) \tag{2.7}$$

Version of June 15, 2019– Created June 15, 2019 - 14:48

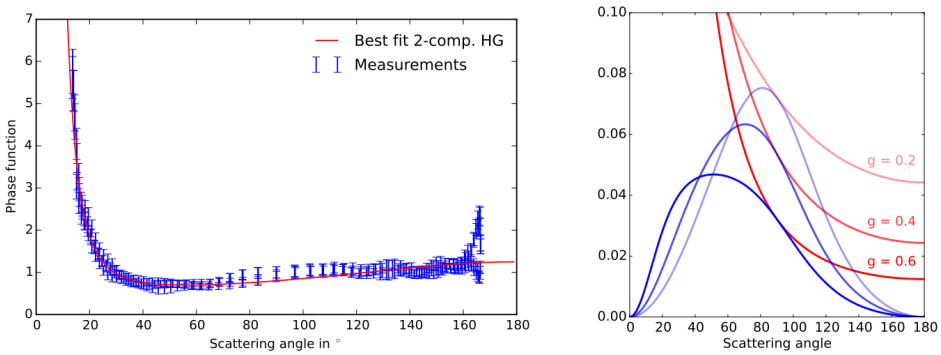

Figure 2.4: Left: *A 2-component Henyey-Greenstein fit by J. Mili et al., 2017 (figure 17) [15] on the scattering phase function of the HR 4796 dust ring in total intensity. The fitted parameters are* $g_{sca} = 0.99^{+0.01}_{-0.38}$ *,* $g_{dif} = -0.14 \pm 0.006$ *, and a weight of w=83%.* ***Right:*** *A model of the scattering phase function for polarized intensities (blue) by N. Engler et al. 2017 (Figure 8) [3] for three different* g_{sca} *parameters. The red lines show the corresponding 1-component Henyey-Greenstein function.*

One reason for a 2-component HG function is that a single HG is a monotonic function, while the SPF of an inclined circumstellar disk is not. This is shown on the left of Figure 2.4. We can use equation 2.7 as a model for the SPF when the surface brightness is computed in total intensity. When we want to compute the surface brightness in polarized intensities we have to adjust the 2-component HG model.

N. Engler et al. argues that the left of Figure 2.4 shows a strong diffraction peak at small scattering angles, $\theta < 30$, and for larger scattering angles a flat scattering intensity profile which is roughly independent of θ. In the 2-component HG function the first part describes the more flat isotropic scattering while the second part contains the sharp diffraction peak. The diffraction peak occurs as light diffracts from large particles (a $>>$ λ), and is expected to produce no polarization. The polarization originates from the scattering of the photons on smaller particles (Rayleigh approximation, a$<<$ λ), and thus is described by the first part of the 2-component HG function for $g_{sca} > 0$. Note that pure forward- or backward scattering does not produce polarized light for randomly orientated dust particles. N. Engler et al. argue that we need to correct the HG model by adding an angular dependence arising from the particle scatterings. The diffraction peak diffracts from the larger particles, so we can assume that the scattered region in the SPF originates from the smaller particles. As a simple

approximation we adopt Rayleigh scattering (see section 2.3.1) to obtain the angular dependence in the polarization fraction p_{sca} (N. Engler et al., 2017 [3]):

$$p_{sca} = p_m \frac{1 - cos^2\theta}{1 + cos^2\theta} = p_m LP(\theta) \tag{2.8}$$

With p_m the scaling factor which defines the maximum fractional polarization produced at a scattering angle of θ= 90°(N. Engler et al., 2017 [3]). Thus the final model to approximate the SPF will be:

$$f(p_m, \theta, g_{sca}) = p_{sca}\, HG(\theta, g_{sca}) \tag{2.9}$$

The right of Figure 2.4 shows some examples of standard f/p_m models for different g values. This gives a visualization of what to expect from the SPF we will compute. Finally, radiative transfer models can link g values to dust properties. One code that is often used is `mcfost` (C. Pinte et al., 2007 [16]), but running these radiative transfer models will be out of the scope of this project and will be left to future work.

2.4 SPHERE/IRDIS Imager

Our observations (see section 3.1) are executed with the (ESO) Very Large Telescope (VLT) in Chile. In order to be able to observe a single protoplanetary disk, we need a high contrast imager. We used the Spectro-Polarimetric High contrast imager for Exoplanets REsearch (SPHERE). The Infra-Red Dual-band Imager and Spectrograph (IRDIS) is a sub-module of SPHERE and is designed to efficiently cover the near-infrared (NIR) range (J. Beuzit et al., 2019 [2]). The basic concept of SPHERE is shown in Figure 2.5. VIS stands for visible wavelengths, while ZIMPOL and IFS are two other sub-modules of SPHERE. SAXO is the high-order extreme Adaptive Optics (AO) system.

In this section, we will describe the optical elements which are most relevant to this research, namely the Half Wave Plate (HWP), and the polarizing beam-splitter of the IRDIS Dual-polarimetry imaging mode (DPI mode).

IRDIS in DPI mode records simultaneously two orthogonal polarization states on the CCD camera (2048X1024 pixels, with a Field of View of 12.27 mas per pixel). This is achieved by using a polarizing beam-splitter. It separates the beam into the vertical and horizontal polarization states by using the angle dependence of the Fresnel equations (equation 2.4). When

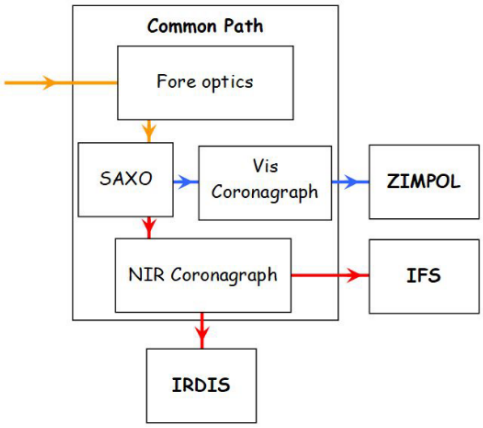

Figure 2.5: *The global concept of the SPHERE instrument, indicating its 4 sub-systems and the main functionalities within the common path sub-system. Optical beams are indicated in orange for VIS+NIR, in blue for VIS and in red for NIR. SAXO is the extreme adaptive optics system of SPHERE. (Figure 1 of J. Beuzit et al., 2019 [2])*

r_p is equal to zero it totally transmits the p-component of the wave. There is a particular angle at which r_p goes to zero, while r_s does not. This angle is called the Brewster angle ($\theta_B = \arctan(n_1/n_2)$, E. Hecht, Optics p348-p350 [10]). The polarized beam-splitter contains a multi-layer dielectric thin film structure on its diagonal face. When the angle of the diagonal face and the incident light ray is equal to the Brewster angle it separates the orthogonal polarization states, as the reflected beam will not contain the p-component of the electric field. This results into two light beams, each containing its own polarization component.

When the beam-splitter is combined with the HWP it enables observations of different polarization orientations. The HWP is as an optical retarder. Retarders change the polarization of the incident wave. The plate causes a phase shift between the s- and p-component (Figure 2.2) by a predetermined amount (E. Hecht, Optics p352[10]). The HWP rotates the orientation of the linear polarized light by twice the angle of the orientation of polarization and the angle of the axis of the HWP. Thus shifting the relative phase of the orthogonal components by 180°. Rotating the HWP at angles: 0°, 45°, 22.5°, and 67.5° aligns different polarization orientations, namely the horizontal-, vertical-, and diagonal orientations, with the axis of the polarizing beam-splitter. When the HWP and the polarized beam-splitter are combined it transforms the degree of polarization per polarization axis to a modulated intensity of the signal.

3 | Methodology

In the following chapter, we will describe which observations are performed in section 3.1 and the data reductions techniques to reduce the data in section 3.2. This will include simple image processing (flat field division, dark- and bad-pixel mask subtraction), Polarimetric Differential Imaging (section 3.2.1) and Reference Differential Imaging (section 3.2.2). Finally, we give a quick introduction on how to do a Bayesian interference with a Markov Chain Monte Carlo simulation in section 3.3.

3.1 PDS 66 observations

The coronagraphic polarimetry images of PDS 66 were observed on 15 and 16 March 2016* under poor weather conditions (SPHERE Manual, 2015 [17]). The observations were made with the Spectro-Polarimetric High contrast imager for Exoplanets REsearch (SPHERE) mounted on the Very Large Telescope in Chile (J. Beuzit et al., 2019 [2]). The observations were part of a large survey implemented by H. Avenhaus et al. 2018 [8]. In this survey were 8 different T Tauri type stars observed, all in IRDIS DPI mode. The details of the observations and the raw data of the PDS 66 are shown in table 3.1 and Figure 3.1, respectively.

3.2 Raw data reduction

The reduction of the DPI data is mainly based on the pipeline C. Ginski created for his 2016 article: "Direct detection of scattered light gaps in the transitional disk around HD 97048 with VLT/SPHERE" [1]. This begins with basic image processes such as flat field division and dark- and bad-pixel mask subtraction. The master bad-pixel mask-, dark-, and flat field files are created with the use of the EsoRex pipeline. The EsoRex pipeline is implemented by the ESO Common Pipeline Library. [18].

3.2.1 Polarimetric Differential Imaging

The goal of Polarimetric Differential Imaging (PDI) is to construct the Stokes I, Q, and U images to determine the intensity and angle of linear polarized light, which arise from scattered starlight of circumstellar disks. To be able to observe such scatter events, the VLT Telescope implemented SPHERE

*Based on observations collected at the European Southern Observatory (ESO) under ESO programme ID: ’096.C-0523(A)

Table 3.1:
Observation executed with the SPHERE/IRDIS imager in DPI mode of PDS 66.

Date (dd-mm-yyyy)	Mode	Filter$^{(*)}$	Exp time (s)	# of expo	$\langle\omega\rangle$ (")	$\langle\tau_0\rangle$ (ms)
15-03-2016	DPI	BB_J	64.0	24	1.5	1.7
16-03-2016	DPI	BB_H	64.0	29	0.94	2.8

Notes. With $\langle\omega\rangle$ the average seeing conditions and $\langle\tau_0\rangle$ the average coherence time. $^{(*)}$ BB_ J, BB_ H means Broadband J, H filter, $\lambda_c = 1245$ nm, $\Delta\lambda = 240$ nm and Broadband H filter $\lambda_c = 1625$ nm, $\Delta\lambda = 290$ nm, respectively [2][8].

with sub-module IRDIS (see section 2.4). One of four different modes of the IRDIS is the DPI mode. In DPI mode the light beam split into two orthogonal polarization directions running parallel through the optical path. Each orthogonal state is then recorded simultaneously on each half of the CCD. We slice the image into two separate intensity frames. We detect the precise center of the star behind the coronagraph with 4 stationary satellite spots created by a waffle pattern applied by the deformable mirror (C. Ginski et al, 2016 [1]). These satellite spots are observed with the telescope in STAR-CENTER mode at the beginning and the end of the observations. The lower image of Figure 3.1 shows these satellite spots. With the help of the EsoRex pipeline we determent the exact position of the center of the star, and aligned the left to the right image.

The Stokes parameters (equation 2.1) describe how to obtain the different polarization images. We have to add the orthogonal polarization states to obtain the total intensity image (Stokes I). So by adding the left to the right frame and taking the median overall observations, we created the final Stokes I image. The Stokes I image is shown in the bottom row of Figure 4.1.

Following equation 2.1 we had to subtract the left from the right frame to obtain the Stokes Q, and U images. The difference in the Q and U images is traced back to the rotation of the Half Wave Plate (HWP). The HWP rotates at angles: 0°, 45°, 22.5°, and 67.5°and thus creating different linear polarization states, namely the Q^+, Q^-, U^+, and U^-, respectively to the orientation of the HWP. The + and - signs refer to the orientation of the polarization (see section 2.1). To correct for internal polarization effects we then simply subtract the Q^-, from the Q^+ image. As a result of the

first subtraction (subtracting the left from the right frame) any astronomical information will possess negative pixel counts for the Q^- image, but the non-common path aberrations have the same sign for the Q^+ and Q^- images (J. Beuzit, et al. 2019 [2]). Thus subtracting the Q^-, from the Q^+ image results in removing the aberrations and obtaining the clean Stokes Q images. The procedure is analog for the Stokes U images. This method is called the double subtraction principle (J. de Boer et al., 2014 [19]).

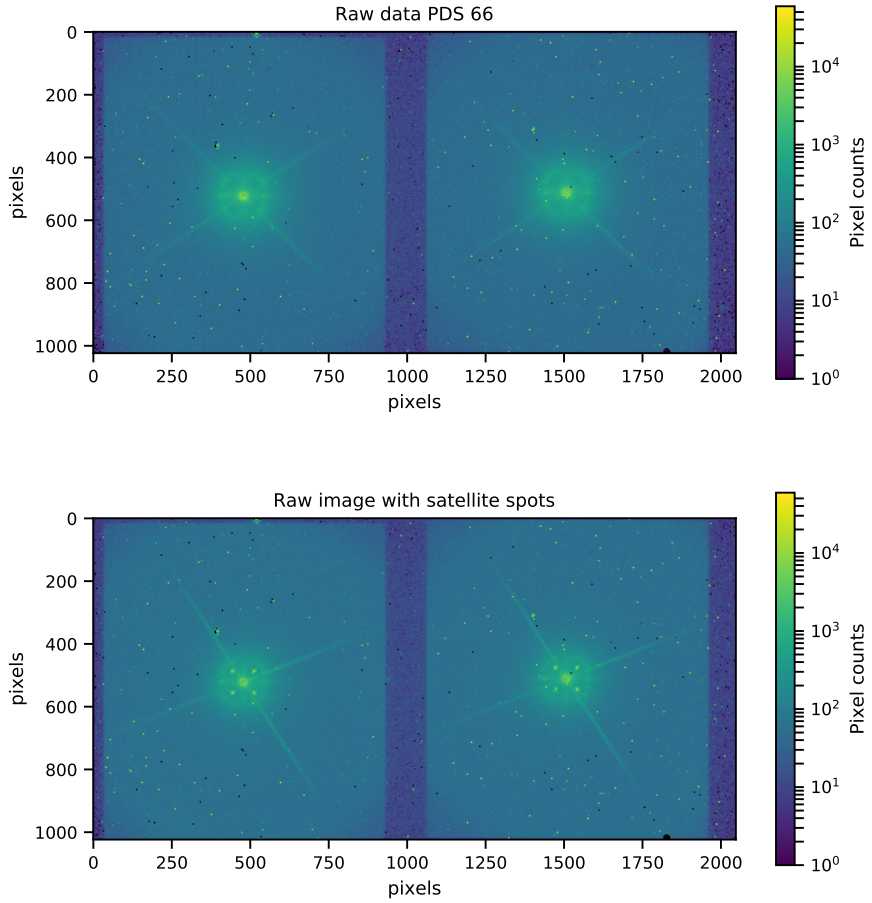

Figure 3.1: *Raw data of the PDS 66 observed in the H-band IRDIS DPI mode. Each pixel corresponds to 12.27 mas.* ***Upper:*** *Raw single exposure science image.* ***Lower:*** *Observations made in STAR-CENTER mode. In this mode are 4 satellite spots created around the coronagraph, to precisely determine the location of the star.*

Since the HWP is only sensitive to instrumental polarization downstream of its position in the optical path, there may still be a small amount of instrumental polarization present in the final Q, and U images (C. Ginski et al., 2016 [1]). To correct for these aberrations we assumed that starlight is unpolarized. The region around the coronagraph can be considered as the overlapping stellar PSF. Then any polarized light just around the coronagraph is caused by internal polarization effects (see section 2.2). To correct for the defects upstream of the HWP we subtracted the degree of polarization around the coronagraph from the Q, and U images. Finally, we have to account for background polarization (i.e. moonlight is polarized light), we took a small aperture outside the accretion disk and subtracted its intensity from the Q, and U images.

To interpreter the data we converted the Stokes Q, and U images to the radial Stokes parameters Q_ϕ, and U_ϕ (H. Schmid et al., 2006 [20]):

$$Q_\phi = +Q\cos 2\phi + U\sin 2\phi \tag{3.1}$$

$$U_\phi = -Q\sin 2\phi + U\cos 2\phi \tag{3.2}$$

Where azimuthal angle ϕ is defined with respect to the star-center. $Q_\phi > 0$ describes an azimuthal polarization, while $Q_\phi < 0$ describes radial polarization. U_ϕ contains all polarizations with 45°from the azimuthal or radial components (C. Ginski et al, 2015 [1]). The reduced images are shown in the top two rows of Figure 4.1.

H. Canovas et al., 2015 [21] confirmed that the U_ϕ images should not include any science material for optically thick protoplanetary disks. Therefore we used the U_ϕ image as a noise map dominated by shot noise and instrumental/data-reduction artifacts (Speckle noise). The noise map is determined by taking one pixel wide annuli around the center of the U_ϕ image and then calculate the standard deviation of each individual annuli. As the U_ϕ image only contains noise, the Q_ϕ image should contain all the signal. The Signal to Noise Ratio (SNR) can thus be determent by $SNR = (\frac{Q_\phi}{noise\ map})^2$. The SNR images of the observations are shown in the third row of Figure 4.1.

3.2.2 Reference Differential Imaging

In order to retrieve the protoplanetary disk in total intensity, we needed to reduce the noise of the stellar flux. In order to reduce the stellar flux we used Reference Differential Imaging (RDI). With RDI you subtract your reference star from your science object to reduce the stellar PSF of the star

(B. Smith et al., 1984 [22]). The total PSF of the image can be described as a linear combination of PSFs from each individual stellar source in an image. With some simplifications, the PSF of PDS 66 can be described as $PSF_{PDS\ 66} = PSF_{starlight} + PSF_{disk} + PSF_{noise}$. The stokes I images are dominated by the PSF of the stellar light. With the use of RDI, we can reduce the PSF of the inner star which results in an image showing the protoplanetary disk in total intensity.

The simplest form of a retrieving the disk is by taking a reduced reference star and simply subtract it from your science object. The reference star must match the stellar PSF of the PDS 66 as close as possible. This includes matching spectral type, apparent magnitude, seeing conditions of the observations, and identical optical paths. The reference star must also be without a circumstellar disk to overcome any over-subtraction in disk signal.

In theory, such an RDI subtraction must be enough to obtain the circumstellar disk, but in practice finding a matching reference star in public data is difficult. Therefore a more complex RDI reduction can be used, for instance, the Principle Component Analysis (PCA). PCA uses a complex algorithm to obtain orthogonal basis of eigen images, on which the science target is projected (R. Soummer, 2012 [23]). Doing a full PCA data reduction is a bachelor thesis on itself. My thesis is about constraining physical processes in protoplanetary disks and thus performing a full PCA analysis is beyond the scope of this project. The results on the simple RDI approach are shown in section 4.2.

3.3 Markov Chain Monte Carlo

We used a Markov Chain Monte Carlo (MCMC) simulation to calculate the likelihood of fitted parameters. In general MCMC simulations are used to approximate basic, possibly high dimensional, integrals in Bayesian interference. Bayesian interference follows the following three postulates (All of Statistics, L. Wasserman p176[24]):

1. Probability describes the strength of belief that the proposition is true.

2. We can make probability statements about parameters, even though they are fixed constants.

3. We make inferences about parameter (θ) by producing a probability distribution for θ. Inferences, such as point estimates and interval estimates, may then be extracted from this distribution.

Bayesian interference is appealing when prior information is available. For the MCMC simulations, we used a least square estimator to compute initial values (prior information). Then with the MCMC we computed, following postulate 3, point estimates and confidence intervals. The package we used to do an MCMC simulation is called: "`emcee`, the MCMC Hammer", by D. Foreman-Mackey et al., 2013 [25].

4 | Results

In this chapter, we applied the theories, models, and data reduction techniques from chapter 2 & 3 to obtain results on the variable illumination regions in the PDS 66 protoplanetary disk. The results are split into three sections: Section 4.1 shows the polarimetric images, section 4.2 the processed RDI images, and section 4.3 contains the results on the SPF.

4.1 PDI images

We used the PDI reduction method, described in section 3.2.1, to obtain the Stokes I, Q_ϕ and U_ϕ images. We illustrate this in Figure 4.1. Figure 4.1 contains polarimetric images in H and J-band on the left and right, respectively. The top row consists the Q_ϕ images, which are build up from the azimuthal polarization directions. The second row contains the U_ϕ images. This is followed up with Signal to Noise Ratio (SNR) in the third row. Section 3.2.1 explains how the SNR is determent. The H-band image contains a higher SNR than the J-band images. Therefore we will only calculate the Scattering Phase Function (SPF) in the H-band. We will expect the SNR of the SPF to be equal to that of Figure 4.1. The final row contains the Stokes I images, which are dominated by the stellar PSF. Under this stellar PSF should be the protoplanetary disk in full intensity. The Stokes I images are used for the RDI reduction.

The variable illumination region is already clearly visible, especially in the Q_ϕ H-band image. Figure 4.2 illustrates the azimuthal profile of the disk polarized intensity surface brightness from 60 - 94 AU (S. Wolff et al, 2019 [26]). It compares two epochs of data; in the middle, the data from the Gemini Planet Imager (GPI), observed on May 2014 by S. Wolff et al. [5], and on the right, the SPHERE data in H-band observed in March 2016. The plot on the left of Figure 4.2 illustrates the gab-like structure (marked with the gray region) between azimuthal angle 160° up to 220°. This corresponds in the GPI data to a drop of 75% in surface brightness, thus confirming the shadow region.

The motion of this region corresponds to a rotational period of roughly 22 years, 30 degrees over 22 months (S. Wolff et al., 2019 [26]). Based on Keplerian motion this could correspond to a planet of a Jupiter-like mass within a 7.5-10 AU radius, which is located within the inner disk. Although, we cannot exclude periods shorter than our single 2 year baseline or verify the direction of motion. Thus the existence of a planet-like object cannot be confirmed and extra observations will be necessary to confirm if the shadow is cast from the inner disk.

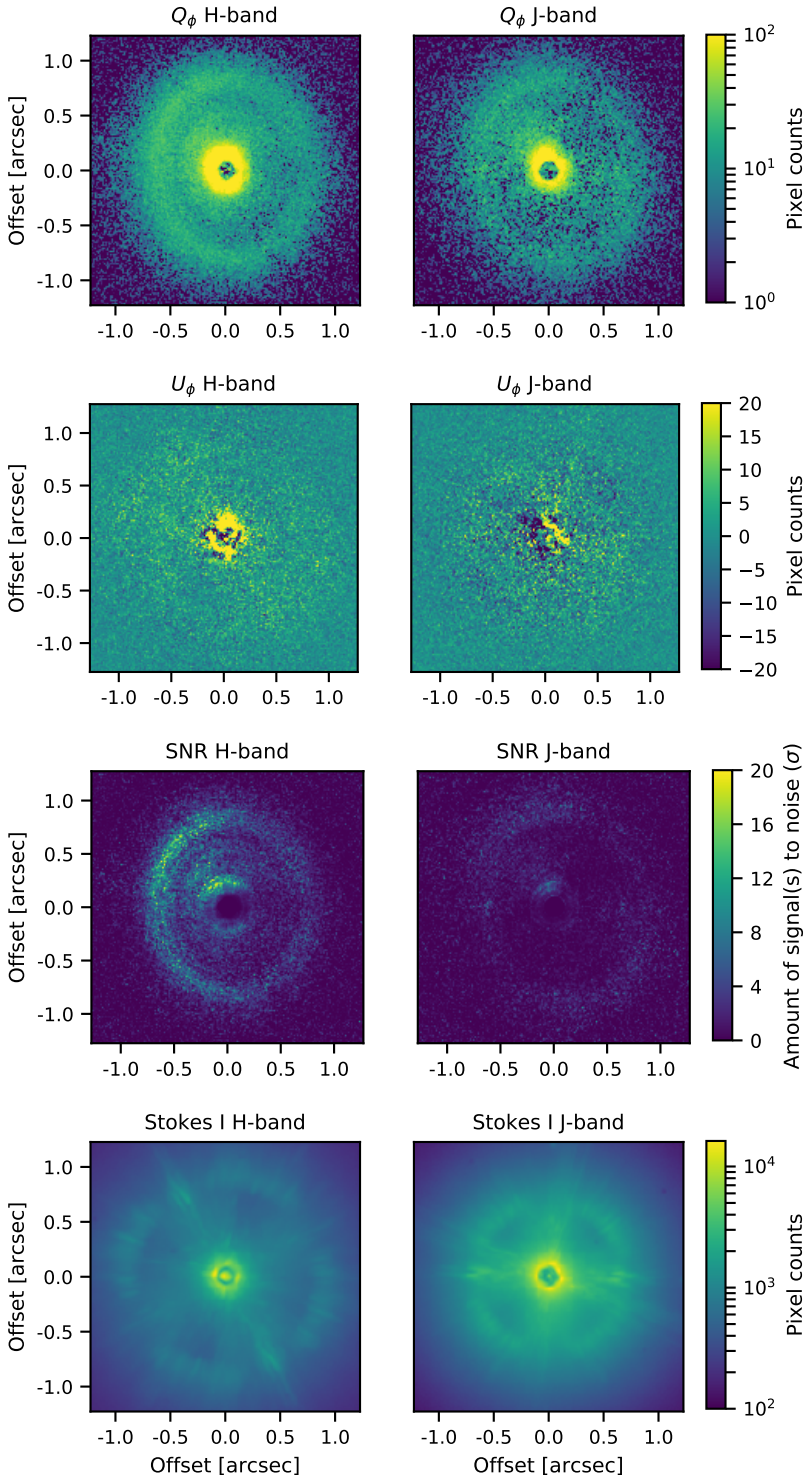

Figure 4.1: *Polarimetric coronagraphic images of the PDS 66 in H- (left) and J-band (right). From top to bottom we have the radial Stokes Q_ϕ, U_ϕ, the SNR and the Stokes I images.*

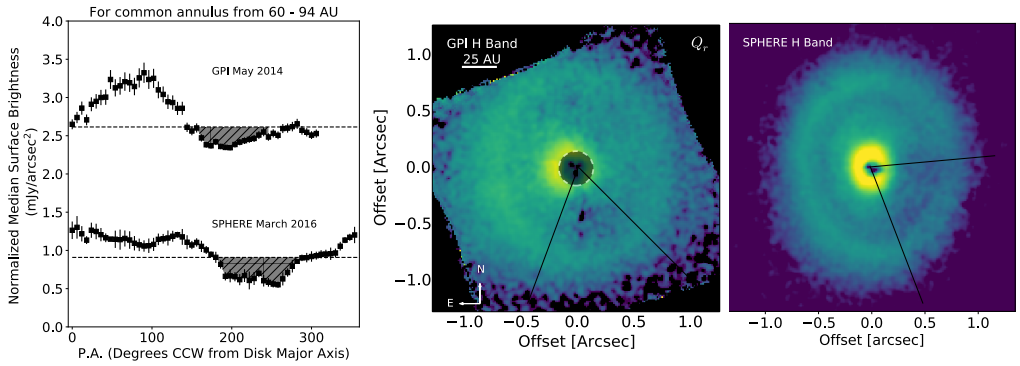

Figure 4.2: *Figure 1 of S. Wolff et al.,2019 [26].* ***Left:*** *The azimuthal profile of existing epochs of polarized intensity data of the PDS 66. The variable illumination region is shaded. The corresponding scattering light regions are shown on the right.* ***Middle:*** *H-band radial Q_ϕ Stokes image obtained with the Gemini Planet Imager in May 2014.* ***Right:*** *H-band radial Q_ϕ Stokes image obtained with SPHERE/IRDIS instrument in March 2016.*

4.2 RDI images

The first step of doing the RDI reduction is to find a suitable candidate. The European Southern Observatory (ESO) in Chile had new PDS 66 observations planned in March, including a suitable reference star observed in IRDIS DPI mode. This reference star was hand-picked and would be ideal for an RDI subtraction, but the observations were postponed and we had to pick reference stars from the ESO archive that satisfied the criteria stated in section 3.2.2.

In total, we looked at more than 300 different candidates all observed with the IRDIS sub-module. We obtained the information on the spectral type and apparent magnitude of the candidates from the SIMBAD astronomical database [27]. No reference star matched the spectral type of the PDS 66, K1-Ve. Thus we chose to use reference stars with spectral type K0 up to M0.

Finally, we decided to only use reference stars which were observed in the same mode as the PDS 66 observations (IRDIS DPI mode) to reduce instrumental artifacts. This only left reference stars with protoplanetary disk as the IRDIS DPI mode is only used for polarimetric observations and observing a single star without a circumstellar disk in DPI mode is not very interesting scientifically. We searched for edge-on, small protoplanetary disks to make sure the reference star did not interfere with the PDS 66

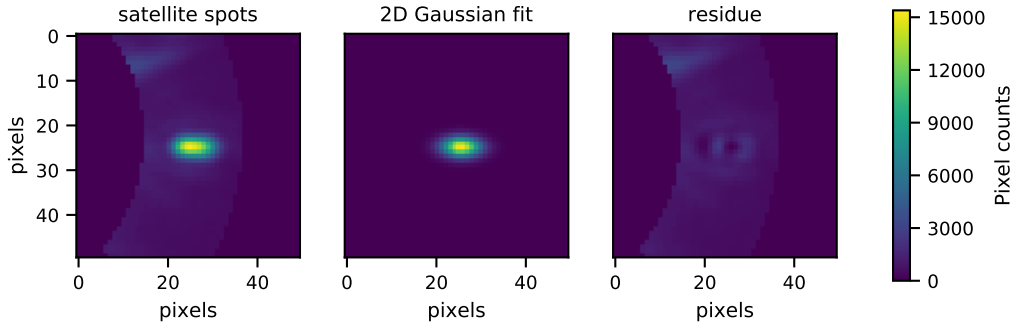

Figure 4.3: *A single sliced satellite spot fitted by a 2D gaussian used to determine the scaling factor between the PDS 66 Stokes I image and the reference star. The scaling factor is determined by taking the median amplitude over all 2D gaussian satellites of the reference star and normalize it by the median amplitude over all PDS satellite fits.* ***Left:*** *One out of four satellite spot as observed in a special OBJECT-CENTER mode of the telescope.* ***Middle:*** *A 2D gaussian fit of the satellite.* ***Right:*** *A residue which originates from subtracting the middle image from the left image.*

disk. This resulted in 11 reference stars. These reference stars are listed in the Appendix A.

To find a matching apparent magnitude was more challenging. We used a scaling factor to match pixel counts and correct for differences in apparent magnitude. We tried different scaling methods. We used, for instance, the FLUX images, which are obtained in a special observation mode without coronagraph, and fitted a 2D gaussian over the stellar PSF. We convoluted these gaussians to match the PSF size and thus correct for different seeing conditions. The relative amplitude of these gaussians, corrected for convolution, was finally used as the scaling factor, but FLUX images have low intensities and thus fitting a 2D gaussian was difficult and eventually unsuccessful. We switched gears and choose to use the satellite spots, which we used earlier to obtain the position of the star behind the coronagraph (section 3.2.1), to determine the scaling factor. The satellite spots are ideal for flux integration as the shape, place, and length of the spots are almost identical for the different reference stars. We again fitted a 2D gaussian on these waffle spots and used the relative amplitude of the gaussians as the scaling factor. Figure 4.3 shows the process of fitting a 2D gaussian on the satellite spots.

Eventually, we did the RDI subtraction with each individual reference star and tried a combination of each reference star by taking the median over all the stars. None showed any significant results. Figure 4.4 shows on the left the Stokes I image in H-band of the PDS 66 and on the right,

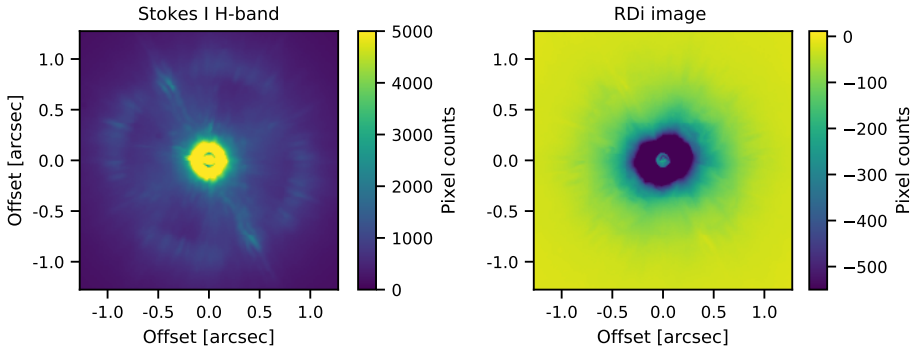

Figure 4.4: Left: *Stokes I image of the PDS 66 in H-band.* ***Right:*** *RDI subtracted image from the Stokes I image of the PDS 66 on the left. The reference star that was used was a median image of a set of 11 different stars, listed in the Appendix A. No disk signal is currently visible on the image on the right, thus the RDI subtraction did not succeed.*

the RDI subtracted version with the median over all candidates as a reference star. The RDI image is over-subtracted and does not contain any disk signal. We conclude that we do not have the data to support basic RDI reduction. In order to further model the protoplanetary disk in full intensity, a hand-picked reference star or a more complex RDI subtraction was necessary, but is beyond the scope of this thesis and will be left for future research.

4.3 Dust properties

To probe dust content we used the polarimetric images. In order to examine the dust properties, we calculated the Scattering Phase Function (SPF). This would give valuable insight on how dust particles scatter light at different positions in the disk. See section 2.3.2 for a more detailed description on the SPF.

The SPF computation is performed in several steps. First, we parameterized the outer ring of the protoplanetary disk, then with equation 2.5, we calculated the scattering angle at each position in the disk which was linked to the surface brightness to obtain the SPF. We interpreted the SPF with an adjusted Henyey-Greenstein (HG) distribution for polarized intensities (equation 2.9). The HG function is described by a single parameter, g, with g defined as the average scattering angle of the dust particles. g-values can be linked to other dust properties with the use of radiative transfer models, but we will leave further modelling to future research and focus only on determining the g-value.

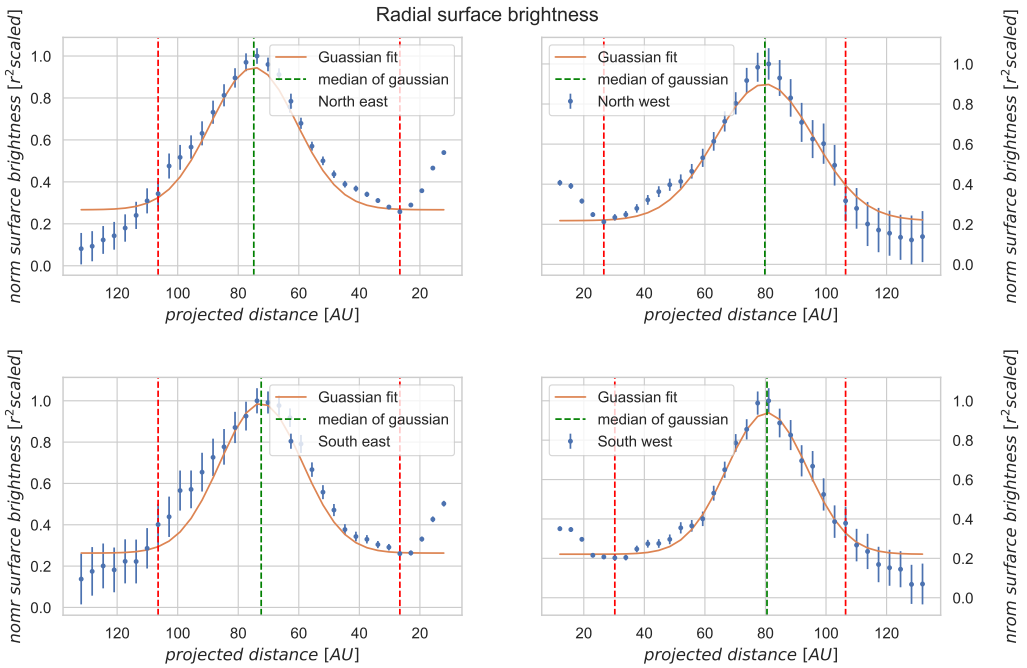

Figure 4.5: *A radial surface brightness profile of the PDS 66 circumstellar disk. The outer ring is fit by a gaussian to determine the location of the center of the outer ring. This location is marked with the middle green dotted line. The gaussians are fit between the outer red dotted lines. The four plots contain the profiles of the northeast, northwest, southeast, and southwest regions of the disk. East is orientated to the left and north upwards.*

First the parameterization of the disk. We only parameterized the outer ring, as the inner ring was more difficult to separate residual stellar polarization from the disk signal. This is due to the method we used to correct for the internal polarization aberrations of the optical path upstream of the Half Wave Plate (see section 5.1 for further discussion).

Protoplanetary disks are circular symmetric when observed face-on. When such a disk is viewed under an angle (the inclination) the circle is tilted and observed as an ellipse. To parameterize the outer ring we have to fit an ellipse through the outer regions of the Q_ϕ image. The ellipse is determent by performing aperture photometry. We binned the azimuthal angle (ϕ) in 10° bins and used radial bins of 3 pixels. This resulted in 36 radial brightness profiles of the tangential polarized intensity. From the luminosity distance relationship ($F \propto 1/r^2$) we can expect the flux from the star to follow the same distribution. Thus we r^2-scaled the radial surface brightness to be able to conduct a better fit through the data. We fitted a single gaussian to the outer disk. This is shown in Figure 4.5. The location

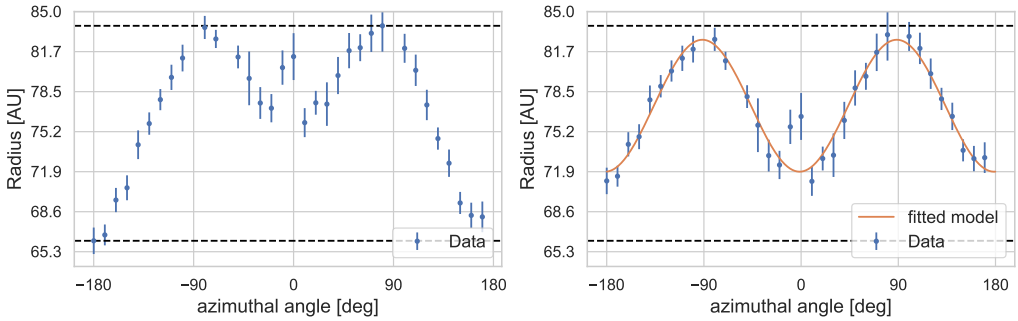

Figure 4.6: Left: *The location of r^2-scaled radial surface brightness peaks with respect to the location of the star, against azimuthal angle (ϕ).* ***Right:*** *The location of r^2-scaled radial surface brightness peaks with respect to the center of the projected ellipse, fitted with a double period sine fit (equation 4.2). The fitted parameters of the sine fit are shown in figure 4.8. The left and right image suggest a stello-centric offset of* 49.8 ± 2.8*mas.*

of the peak of this gaussian should follow an ellipse. Thus plotting the azimuthal angle against the median of the gaussians should result in a sine function with a double period. The left of Figure 4.6 shows these results. The data shows a clear offset at angel $0°$ and $\pm\, 180°$, which is due to a shift in the center of the ellipse relative to the location of the star. A shift in the x-axis should correspond to half the difference in amplitude, but it should not create a shift in the peak values of the data. This pattern follows a sine function. We can have an offset in the y- and x-axis, so the model we used to obtain the center of the ellipse is a superposition of a sine and a cosine:

$$f_{center}(\phi, x_c, y_c, \Phi) = y_c \cos(\phi + \Phi) + x_c \sin(\phi + \Phi) \tag{4.1}$$

With ϕ the azimuthal angle, y_c and x_c the stello-centric offset in the y and x-directions, and Φ the phase of the total sine fit used to fit the median of the gaussians against the azimuthal angle. The total sine fit is defined as follows:

$$f_{sin}(\phi, A, \Phi, x_c, y_c) = A \sin(2\phi + \Phi) + h + f_{center} \tag{4.2}$$

With h the mean radius of the disk, and A the amplitude of the sin fit.

We computed a MCMC simulation to obtain the best-fitted values and the likelihood on each parameter of the sine fit. The fitted model with the center corrected data (adjusted chi squared of $\chi^2 = 0.80$) is shown on the right of Figure 4.6. The two data points at $\phi = 0$ are excluded from the MCMC simulation.

Version of June 15, 2019– Created June 15, 2019 - 14:48

We translated the parameters of the fitted sine model to the parameterization of the ellipse. The phase (Φ) corresponds to the Position Angle (PA); The mean radius of the ellipse $\pm$ the Amplitude correspond to the semi-major (a) and minor (b) axis of the ellipse respectively; and the inclination is defined as $i = \arccos(b/a)$. Table 4.1 shows the fitted parameters with 1σ uncertainty. The ellipse is visualized in Figure 4.7, showing the fitted ellipse on the left and the corresponding SNR map on the right. The width of the outer ring is determined by the Full Width Half Maximum (FWHM) of the r^2-scaled radial surface brightness gaussian fits at 33.5 AU.

We eventually performed the parametrization of the ellipse twice. In order to r^2-scale the image we had to deproject the ellipse to a circle and to deproject the ellipse we needed the parametrization of the ellipse. We first fitted a gaussian to the radial surface brightness profile without r^2-scaling, to obtain a rough estimate of the parameters of the ellipse. We used these parameters to deproject and r^2-scale the Q_ϕ image which let to the results shown in Figure 4.6, 4.7, 4.8, and table 4.1. Figure 4.8 is a contour plot of the 2-dimensional likelihood of the fitted parameters. The uncertainties correspond to $\pm 1\ \sigma$.

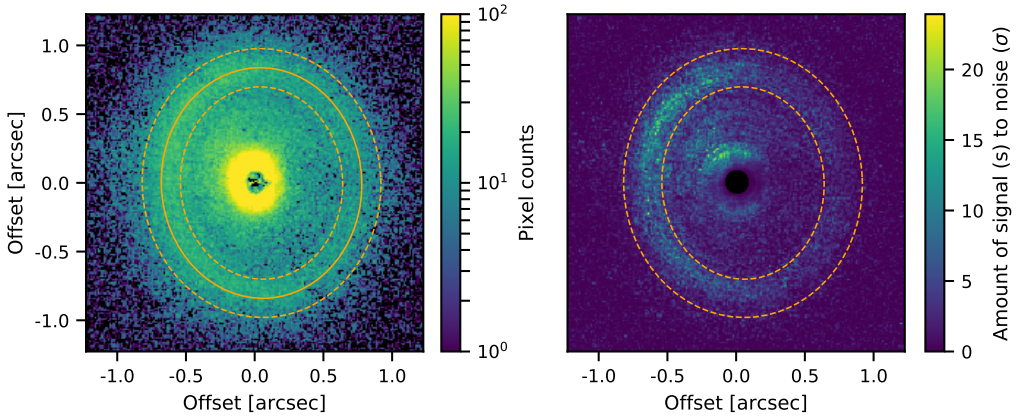

Figure 4.7: Left: *The radial H-band Q_ϕ Stokes image of the PDS 66. The solid orange line represents the ellipse with the best-fitted parameters shown in table 4.1. The width of the dashed lines corresponds to the FWHM of the fitted gaussian over the radial surface brightness profile shown in Figure 4.5.* ***Right:*** *The SNR map of the PDS 66 with the same ellipse plotted as in the left figure.*

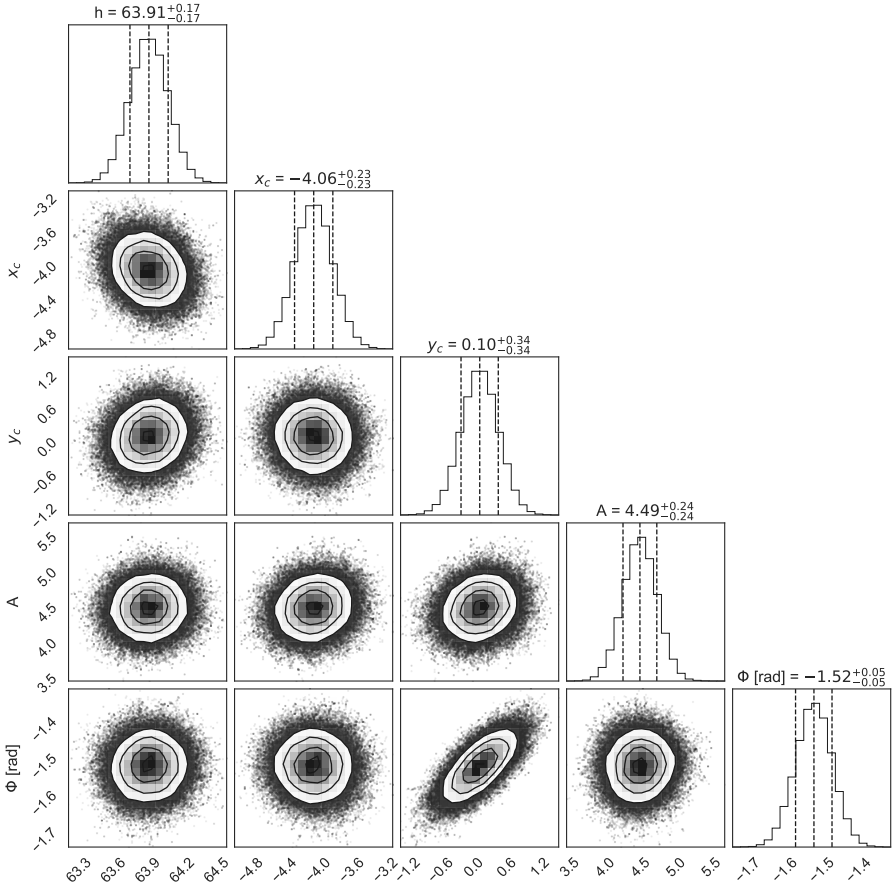

Figure 4.8: *A contour plot of the 2D likelihood of the fitted parameters from the sine fit shown in Figure 4.6. With h the mean radius of the disk, and A the amplitude of the sin fit, x_c and y_c the stello-centric offset in x- and y-directions, and Φ the phase of the sin fit. All the parameters are expressed in pixel ranges, except the phase which is expressed in radiance. The uncertainties correspond to $\pm 1\sigma$.*

parameters ellipse	best-fitted value	1σ uncertainty
a (arcsec)	0.839	0.004
b (arcsec)	0.729	0.004
i (°)	29.6	0.7
PA (°)	2.8	2.8
Δx center (mas)	-49.8	2.84
Δy center (mas)	1.2	4.1

Table 4.1: *The best-fitted parameters of the ellipse, which characterizes the outer disk of the PDS 66.*

With the parametrization of the ellipse we calculated the scattering angle (θ), with equation 2.5. The SPF was obtained by linking θ with the surface brightness. We determined the surface brightness per scattering angle by slicing the outer ring in azimuthal angles of 1° and we integrated over the area. This resulted in the total flux per azimuthal angle for the outer ring. Figure 4.9 shows the surface brightness profile for polarized intensities of the north and south side of the outer disk fitted with function 2.9. The SPF are individually normalized for the north and the south by taking the surface brightness at a scattering angle of 90°. We found a $\approx$ 30% increase in surface brightness for the north compared to the south side of the disk at these scattering angles.

Figure 4.10 shows the corner plot of the MCMC simulation of the corrected HG model with the best-fitted parameters of the ellipse on the north (left) and south (right) side of the disk. To obtain the uncertainties of the adjusted HG model we deviated the determent parameters of the ellipse, used to characterize the outer ring, by $\pm 1\sigma$ when calculating the SPF. Table 4.2 shows the results on the best-fitted parameters with their respective uncertainties.

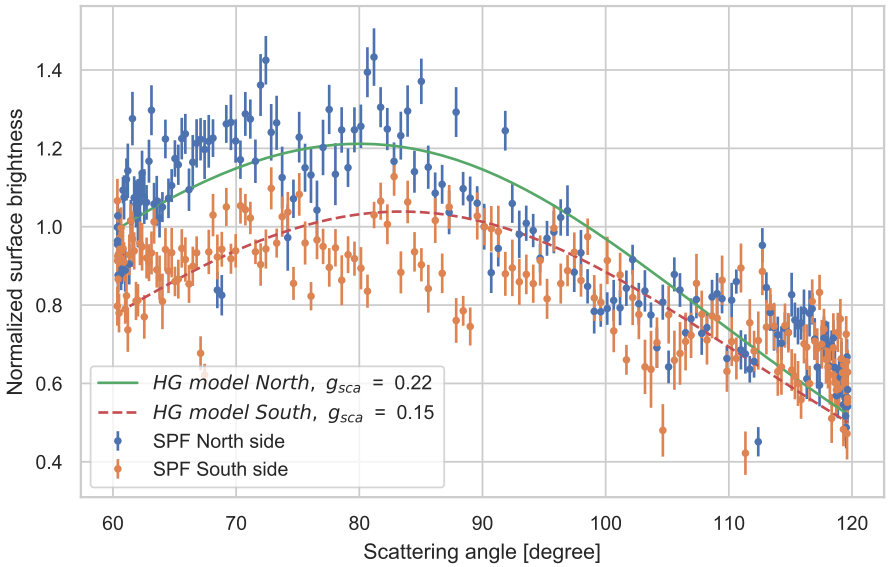

Figure 4.9: *The Scattering Phase Function (SPF) of the PDS 66 for the north (blue) and south (orange) side of the disk. An adjusted Henyey-Greenstein distribution for polarized intensities (equation 2.9) is used to model the SPF for the north (green, solid) and south (red, dashed) side. The SPFs are normalized at a scattering angle of* 90° *for the north and south side individually.*

	g_{sca}	p_m	χ^2
North	$0.22^{+0.02}_{-0.02}$	$16.34^{+01.05}_{-01.55}$	5.69
South	$0.15^{+0.02}_{-0.01}$	$13.47^{+05.21}_{-00.06}$	6.35

Table 4.2: *The best-fitted parameters of the surface brightness profile with an adjusted Henyey-Greenstein distribution for polarized intensities, equation 2.9. The uncertainties are determined by deviating the fitted parameters of the ellipse, used to characterize the outer ring of the disk, by $\pm 1\sigma$ while calculating the scattering phase function.*

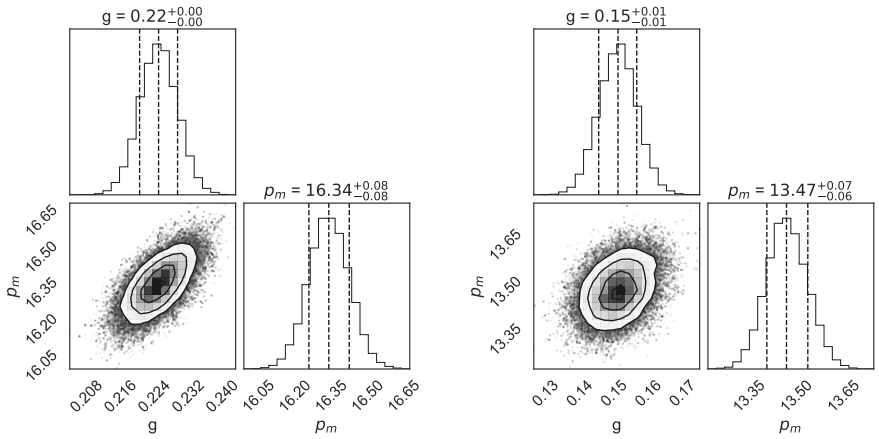

Figure 4.10: *A contour plot of the 2D likelihood of the fitted parameters from an adjusted Henyey-Greenstein (HG) distribution of polarized intensities from the best-fitted parameters of the ellipse shown in table 4.1. The uncertainties on top of the corner plot correspond to $\pm 1\sigma$ of the determent likelihood.*

Version of June 15, 2019– Created June 15, 2019 - 14:48

5 | Discussion

In this section, we will discuss the results which were obtained in section 4. The discussion of the results is split in two. First the discussion on the PDI images in section 5.1, then in section 5.2, we elaborate on the analysis on the results of the dust properties. Finally, in section 5.3, we discuss future directions on possible research.

5.1 Systematic noise in the PDI images

The first results we obtained were the polarimetric images of the PDS 66. The PDS 66 shows a close resemblance to other face-on protoplanetary disks, like the TW Hydra (c. Poteet et al., 2018 [4]), in its ring-like structures. Figure 4.1 shows the PDI images of the PDS 66.

The second row of Figure 4.1 contains the U_ϕ images in H- and J-band. Section 3.2.1 describes that the U_ϕ image should be dominated by systematic noise (shot noise) and instrumental/data-reduction artifacts. If the noise was dominated by shot noise, than there must be a more Poisson-like distribution centered around zero. Compare the J-band image (right) to the H-band image (left), and we observe that the J-band image shows more negative pixel counts than the H-band image. Thus the U_ϕ H-band image is more dominated by instrumental/data-reduction artifacts, especially in the inner regions around the coronagraph. This corresponds to overleaping stellar flux, indicating that our Q_ϕ data is containing these aberrations as well. The internal polarization correction upstream of the HWP (see section 3.2.1) is most likely the cause of these aberrations as it is less accurate than the use of a fully computed Mueller matrix.

5.2 Dust characterization analysis

To obtain the scattering phase function, we characterized the outer disk of the ellipse by fitting a double period sine function through the position of the radial surface brightness peak per azimuthal angle (see Figure 4.6). This fit suggested an offset between the center of the star, and the location of the center of the fitted ellipse by 49.8 ± 2.8mas. This offset suggests a more flared primordial disk then what was expected by S. Cortes et al., 2009 [6], and S. Wolff et al., 2016 [5], although the stello-centric offset is still consistent with the findings of G. Schneider et al., 2014 [28].

When we compare the fitted parameter of the ellipse (table 4.1) with other literature we found that it agrees well with the GPI data ($i = 31^\circ \pm$

2°, PA = 10° ± 3° S. Wolff et al., 2016 [5]), and the Hubble data ($i = 27°3 \pm 3°3$, G. Schneider et al., 2014[28]), and we found that it relates very closely to the SPHERE data processed by H. Avenhaus et al., 2018 [8] ($i = 30°26 \pm 0°88$, PA $= 189°19 \pm 1°33$). The GPI, Hubble, and the SPHERE (by H. Avenhaus et al.) characterizations of the ellipse were obtained by a direct fit on the brightness contours in the image with the use of a non-linear least square estimator, and not with the double period sine method we used for our data processing.

Furthermore, fitting the adjusted Henyey-Greenstein model (equation 2.9) was challenging. The minimum and maximum scattering angles are defined by $\theta = 90 \pm i$. Therefore the face-on nature of the disk made it impossible to reach the high and low scattering angles. The range in scattering angle of the PDS 66 is from 60° up to 120°, which corresponds to half the total range of the model, which is shown on the right of Figure 2.4. This made fitting the shape of the adjusted HG model difficult which translates into the chi squared values. We found, when calculating the uncertainties, that the HG model was most sensitive to the changes in the PA of the disk.

The last phenomena we noticed was a higher surface brightness in the north relative to the south side of the outer disk at scattering angles of 90°. We expect for $g_{sca} > 0$ an increase in surface brightness for smaller scattering angles, as dust particles in protoplanetary disk tend to prefer forward scattering over backward scattering (S. Wolff et al., 2016[5]; J. Mili et al., 2017 [15]; N. Engler et al., 2017 [3]), but we found a $\approx$ 30% higher surface brightness on the north compared to the south side of the disk, which in theory should be identical (Henyey & Greenstein, 1941[14], J. Mili et al., 2017 [15]). Both regions are located outside the shadow and thus can be ruled out as an explanation. H. Avenhaus et al., 2018 [8] observed these enhancements as well and claims that it is due to the maximized polarizing efficiency at scattering angle of 90 °, but a more detailed model of the intensity profile of the disk must be computed to give further insight in the scattering properties of the dust particles throughout the disk.

5.3 Future directions

For future research we advise, a more detailed internal polarization correction with the use of a fully build Mueller matrix. This would disentangle the overleaping stellar flux around the coronagraph, and improve the SNR of the inner regions of the PDI images. The RDI reduction will become less noise sensitive, due to the improved internal polarization aberrations, and

in combination with a PCA analysis could be enough to obtain the disk signal in total intensity with the data from the public archive. We expect the total intensity in the outer ring to be roughly 5 pixel counts per seconds (320 pixel counts for an integration time of 64 seconds) for scattering angles of 90°, as we simulated the maximum fractional polarization (p_m) at scattering angles of 90°, with the adjusted Henyey-Greenstein function. The total intensity image would give more insight into the polarization fraction and surface brightness asymmetries, leading to a more detailed characterization of the dust properties and local scale height variations in the inner disk.

Another option to retrieve the image in total intensity is to use a hand-picked reference star. Combining the observation of this reference star with new observations on the PDS 66 would increase the 2 year baseline on the rotational timescales. Link the rotational time-scales with the resolved total intensity image and it could provide valuable new means on investigating physical processes in the inner disk.

Finally, a more complete SED or improved image modeling (like the HIP 79977 intensity modeling, by N. Engler et al., 2017 [3]) should be made to confirm the stello-centric offset, discussed in section 5.2 and further discuss the flaring exponent and flatness of the disk. Such a model would also give insight on whether an adjusted Henyey-Greenstein distribution was a proper method on probing dust content, as better fits with lower χ^2-values could be obtained.

6 | Conclusion

The goal of this thesis was to explore the gab- and ring-like structures in the protoplanetary disk of the PDS 66, which could provide valuable new means on investigating physical processes inherent in terrestrial planet formation. We wanted to explore these variable illumination regions by first performing Polarimetric Differential Imaging (PDI) and thus obtaining the Stokes Q, U, and I images (Figure 4.1). Via RDI we wanted to resolve the disk in total intensity. Our results showed that performing an RDI subtraction with a reference star build up from the public ESO archive was unsuccessful. As observations in March 2019 were postponed, and thus missing out on an ideal hand-picked reference star, we did not have the data to support a simple RDI reduction. We leave forward modeling of the disk's surface brightness in total intensity to future work.

However, we computed a rough estimation on the polarization fraction (p_m) at a 90° scattering angle, not by obtaining the disk signal in total intensity, but by fitting an adjusted Henyey-Greenstein (HG) model for polarized intensities (equation 2.9) to the scattering phase function. We found $p_m = 16.33$ for the north side of the disk and a $p_m = 13.49$ for the south side. This corresponds to roughly 5 pixel counts per second in the outer disk (320 pixel counts for an integration time of 64 seconds), when the disk's surface brightness is obtained in total intensity.

Fitting the HG model to the scattering phase function to probe dust content was our second goal. In order to fit the HG, we first confirmed literature results on the inclination and position angle of the outer disk with the double period sine method (section 4.3). With this method, we found a stello-centric offset of 49.8 ± 2.8mas which could suggest a larger flaring angle than expected in previous literature. The results on the adjusted HG model were $g_{sca} = 0.22 \pm 0.02$ and $g_{sca} = 0.15 \pm 0.02$ and suggest different dust properties for the north- compared to the south side of the disk.

Our third and final goal was linking SPHERE data with the GPI data to obtain dynamical timescales on processes in the inner regions of the disk. Again, due to the postponed observations in March, we only had two epochs of data in polarized intensities with a baseline of 22 months. Thus we cannot exclude a rotational period shorter than our roughly 2 year baseline or confirm the direction of rotation. Even though the two epochs correspond to a rotational period of roughly 22 years (30° over 22 months, see Figure 4.2). Based on Keplerian motion, this rotation is consistent with planets of Jupiter-like mass within a 7.5-10 AU radius, which is located inside the inner disk.

Bibliography

[1] C. Ginski et al., *Direct detection of scattered light gaps in the transitional disk around HD 97048 with VLT/SPHERE*, Astronomy & Astrophysics **595**, A112 (2016).

[2] J.-L. Beuzit et al., *SPHERE: the exoplanet imager for the Very Large Telescope*, Technical report, 2019.

[3] N. Engler et al., *The HIP 79977 debris disk in polarized light*, Astronomy & Astrophysics **607**, A90 (2017).

[4] C. A. Poteet, C. H. Chen, D. C. Hines, M. D. Perrin, J. H. Debes, L. Pueyo, G. Schneider, J. Mazoyer, and L. Kolokolova, *Space-based Coronagraphic Imaging Polarimetry of the TW Hydrae Disk: Shedding New Light on Self-shadowing Effects*, The Astrophysical Journal **860**, 115 (2018).

[5] S. G. Wolff et al., *the Pds 66 Circumstellar Disk As Seen in Polarized Light With the Gemini Planet Imager*, The Astrophysical Journal **818**, L15 (2016).

[6] S. R. Cortes, M. R. Meyer, J. M. Carpenter, I. Pascucci, G. Schneider, T. Wong, and D. C. Hines, *Grain growth and global structure of the protoplanetary disk associated with the mature classical t tauri star, PDS66*, Astrophysical Journal **697**, 1305 (2009).

[7] G. Collaboration et al., *Baker 22 , L. Balaguer-Núñez 11 , P. Balm 20 , C. Barache 29 , C. Barata 45 , D. Barbato 66, 23 , F. Barblan 9*, Technical report, 2018.

[8] H. Avenhaus, S. P. Quanz, A. Garufi, S. Perez, S. Casassus, C. Pinte, G. H-M Bertrang, C. Caceres, M. Benisty, and C. Dominik, *Disks around T Tauri Stars with SPHERE (DARTTS-S). I. SPHERE/IRDIS Polarimetric Imaging of Eight Prominent T Tauri Disks **, (2018).

[9] C. Marois, D. Lafreniere, R. Doyon, B. Macintosh, and D. Nadeau, *Angular differential imaging: a powerful high-contrast imaging technique*, The Astrophysical Journal **641**, 556 (2006).

[10] E. Hecht and A. Zajac, *Optics addison-wesley*, Reading, Mass **19872**, 350 (1974).

[11] G. S. University, *Classification of Polarization*, 2019.

[12] J. B. Breckinridge, W. S. T. Lam, and R. A. Chipman, *Polarization aberrations in astronomical telescopes: the point spread function*, Publications of the Astronomical Society of the Pacific **127**, 445 (2015).

[13] U. o. A. Griffith, *Incident Light 1.1. Phase Function Definition*, 2019.

[14] L. G. Henyey and J. L. Greenstein, *Diffuse radiation in the galaxy*, The Astrophysical Journal **93**, 70 (1941).

[15] J. Milli et al., *Near-infrared scattered light properties of the HR 4796 A dust ring-A measured scattering phase function from 13.6Â° to 166.6Â°*, Astronomy & Astrophysics **599**, A108 (2017).

[16] C. Pinte, L. Fouchet, F. Ménard, J.-F. Gonzalez, and G. Duchêne, *On the stratified dust distribution of the GG Tauri circumbinary ring*, Astronomy & Astrophysics **469**, 963 (2007).

[17] D. Mawet, J. Girard, Z. Wahhaj, and M. Van Den Ancker, *SPHERE User Manual*, (2015).

[18] E. S. O. (ESO), *The Common Pipeline Library*, 2019.

[19] J. de Boer, J. H. Girard, D. Mawet, F. Snik, C. U. Keller, and J. Milli, *Characterizing instrumental effects on polarization at a Nasmyth focus using NaCo*, **9147**, 914787 (2014).

[20] H. M. Schmid, F. Joos, and D. Tschan, *Limb polarization of Uranus and Neptune I. Imaging polarimetry and comparison with analytic models*, A&A **452**, 657 (2006).

[21] H. Canovas, F. Ménard, J. de Boer, C. Pinte, H. Avenhaus, and M. Schreiber, *Nonazimuthal linear polarization in protoplanetary disks*, Astronomy & Astrophysics **582**, L7 (2015).

[22] B. A. Smith and R. J. Terrile, *A circumstellar disk around Beta Pictoris*, Science **226**, 1421 (1984).

[23] R. Soummer, L. Pueyo, and J. Larkin, *Detection and characterization of exoplanets and disks using projections on Karhunen-Loève eigenimages*, The Astrophysical Journal Letters **755**, L28 (2012).

[24] L. Wasserman, *All of statistics: a concise course in statistical inference*, Springer Science & Business Media, 2013.

[25] D. Foreman-Mackey, D. W. Hogg, D. Lang, and J. Goodman, *emcee: the MCMC hammer*, Publications of the Astronomical Society of the Pacific **125**, 306 (2013).

[26] E. Organisation, S. Hemisphere, and I. Notice, *European Organisation for Astronomical Research in the Southern Hemisphere Important Notice : PERIOD : Category : C â 4 Special remarks : Principal Investigator : (moved to the CoI list) B â Immediate Objective :*, page 1 (2020).

[27] M. Wenger, F. Ochsenbein, D. Egret, P. Dubois, F. Bonnarel, S. Borde, F. Genova, G. Jasniewicz, S. Laloë, S. Lesteven, and R. Monier, *The SIMBAD astronomical database. The CDS reference database for astronomical objects*, **143**, 9 (2000).

[28] G. Schneider, C. A. Grady, D. C. Hines, C. C. Stark, J. H. Debes, J. Carson, M. J. Kuchner, M. D. Perrin, A. J. Weinberger, J. P. Wisniewski, M. D. Silverstone, H. Jang-Condell, T. Henning, B. E. Woodgate, E. Serabyn, A. Moro-Martin, M. Tamura, P. M. Hinz, and T. J. Rodigas, *PROBING FOR EXOPLANETS HIDING IN DUSTY DEBRIS DISKS: DISK IMAGING, CHARACTERIZATION, AND EXPLORATION WITHHST/STIS MULTI-ROLL CORONAGRAPHY*, The Astronomical Journal **148**, 59 (2014).

A | Reference stars

Here we list the reference stars used for the RDI subtraction. The results are shown in Figure 4.4. We selected the reference stars on the criteria discussed in section 4.2. The bottom row of table A.1 contains the PDS 66 observations for comparison.

Table A.1:
A base of all the reference stars used for the RDI subtraction

Name	Spectral Type	Total obs. time (s)	Scaling factor$^{(\dagger)}$	$\langle\omega\rangle$ (")	Date obs. (yyyy-mm-dd
2MASS J16$^{(*)}$	K2	1792	5.94	0.80 [0.01]	2017-06-18
AS 209	K4Ve	544	1.46	1.00 [0.05]	2016-03-15
DoAr 44	K3e	1280	4.33	1.01 [0.09]	2016-03-16
EX Lup	M0	1536	9.37	1.23 [0.31]	2017-05-16
GM Aur	K3Ve	2048	16.8	0.60 [0.01]	2018-01-02
IRAS 08267-3336	K2.0	1156	25.5	0.74 [0.01]	2017-05-15
MY Lup	K0	1408	4.97	0.77 [0.01]	2016-03-16
SY Cha	K5Ve	2048	9.93	0.76 [0.01]	2017-05-16
TW Hya	K6Ve	1648	4.87	0.73 [0.01]	2015-04-01
T Cha	K0e	3840	7.79	1.16 [0.30]	2016-02-20
UX Tau A	K2Ve	2560	12.4	0.86 [0.04]	2017-10-06
PDS 66	K1Ve	1856	- -	1.05 [0.12]	2016-03-16

Notes. $^{(*)}$ Full name is 2MASS J16083070-3828268. $^{(\dagger)}$ The scaling factors are corrected for their exposure times. $\langle\omega\rangle$ corresponds to the average seeing conditions, with a 1σ error estimation within the brackets. All observations are made in IRDIS/DPI mode with broadband filter BB_H, this relates to $\lambda_c = 1625$ nm, $\Delta\lambda = 290$ nm. The information on the observations is gathered from the header of the fits files or from the Simbad Archive [18].